Biophysical *Journal*
Article

Biophysical Society

Quantitative imaging of *Caenorhabditis elegans* dauer larvae during cryptobiotic transition

Kyoohyun Kim,[1,2] Vamshidhar R. Gade,[3] Teymuras V. Kurzchalia,[3,*] and Jochen Guck[1,2,*]
[1]Biotechnology Center, Center for Molecular and Cellular Bioengineering, Technische Universität Dresden, Dresden, Germany; [2]Max Planck Institute for the Science of Light & Max-Planck-Zentrum für Physik und Medizin, Erlangen, Germany; and [3]Max Planck Institute of Molecular Cell Biology and Genetics, Dresden, Germany

ABSTRACT Upon starvation or overcrowding, the nematode *Caenorhabditis elegans* enters diapause by forming a dauer larva, which can then further survive harsh desiccation in an anhydrobiotic state. We have previously identified the genetic and biochemical pathways essential for survival—but without detailed knowledge of their material properties, the mechanistic understanding of this intriguing phenomenon remains incomplete. Here we employed optical diffraction tomography (ODT) to quantitatively assess the internal mass density distribution of living larvae in the reproductive and diapause stages. ODT revealed that the properties of the dauer larvae undergo a dramatic transition upon harsh desiccation. Moreover, mutants that are sensitive to desiccation displayed structural abnormalities in the anhydrobiotic stage that could not be observed by conventional microscopy. Our advance opens a door to quantitatively assessing the transitions in material properties and structure necessary to fully understand an organism on the verge of life and death.

SIGNIFICANCE When exposed to harsh environments, some organisms enter a dormant state and survive almost complete desiccation. So far, this phenomenon has only been investigated from a genetic and biochemical viewpoint. But why do organisms not crumble to dust when dried out? How can they stay structurally and functionally intact and resume after adding water, as if nothing special occurred? Such a feat surely requires peculiar material properties. However, we know little about the accompanying structural changes, and quantitative transitions in material properties, for lack of appropriate tools. Here we demonstrate that ODT can address this need and open the door toward better understanding the maintenance of organismal integrity in transitions between life and death.

INTRODUCTION

To withstand fluctuations in environmental conditions, organisms have developed various strategies. One such strategy is entering a dormant state. The extreme form of dormancy is cryptobiosis (hidden life), when the metabolism of an organism under conditions that are not compatible with life (no food, no water or oxygen, very high or low temperatures, high osmotic pressure, etc.) is reduced to an undetectable level. Upon encountering favorable conditions, the organism exits the cryptobiotic state and resumes metabolism and other vital activities. Prominent examples of cryptobiosis are survival of dry bacterial or fungal spores, dormant plant seeds, or the ability of tardigrades and some nematodes to survive desiccation (1–5). Studying the molecular, structural, and material mechanisms that accompany this reversible cryptobiotic transition, is fundamental for identifying the essential differences between the living and the dead state of an organism.

In the past decade, the nematode *Caenorhabditis elegans* has been established as a model for studying one form of cryptobiosis—anhydrobiosis (life in the absence of water) (6). Under favorable conditions, *C. elegans* goes through the reproductive life cycle where a fertilized egg develops through larval stages from L1 to L4 to a reproductive adult. However, when encountering a harsh environment, overcrowding, or food scarcity, *C. elegans* pauses the reproductive cycle and enters diapause by forming a nonfeeding dauer larva (7). It has been shown that this dauer larva can survive severe desiccation (6), high osmotic pressure, or

Submitted September 30, 2021, and accepted for publication February 16, 2022.

*Correspondence: kurzchalia@mpi-cbg.de or jochen.guck@mpl.mpg.de

Vamshidhar R. Gade present address is Institute of Biochemistry, ETH Zürich, 8093 Zürich, Switzerland.

Kyoohyun Kim and Vamshidhar R. Gade contributed equally.

Editor: Catherine Galbraith.

https://doi.org/10.1016/j.bpj.2022.02.031

© 2022 Biophysical Society.

This is an open access article under the CC BY license (http://creativecommons.org/licenses/by/4.0/).

freezing (8). The dauer larvae differ from reproductive larvae in both metabolism and morphology (7,9). They have reduced metabolic activity (oxygen consumption rate, heat production), and as a nonfeeding stage, they mostly rely on internal reserves (triacylglycerols) by using glyoxylate shunt to synthesize sugars (9). Morphologically, they differ from reproductive larvae by a significant reduction in volume, which is a result of a radial shrinkage during the formation of the dauer larva.

In order to survive harsh desiccation, dauer larvae first need to be exposed to a mild decrease of relative humidity (RH), a process called preconditioning. Previously, we identified genetic and biochemical pathways that are activated during the preconditioning (10) and are crucial for survival. Among these are the many-fold increase of a disaccharide trehalose and massive biosynthesis of an intrinsically disordered protein LEA-1 (6,10). Despite this increasing insight into genetic and biochemical details, only very little is known about the actual morphological and material changes that enable the successful survival during reversible transitions. Only some gross anatomic changes, such as a reduction of the overall volume of the worms, have been reported (11,12). The detailed structural changes that take place inside the animal have been elusive because it is notoriously difficult to reliably image the process of desiccation or a desiccated worm both with fluorescence and electron microscopy. Going beyond structure, it has not been feasible so far to quantitatively map the distribution of the material properties inside the worm, which accompany, and arguably enable, the intriguing transitions between metabolically active and inactive states, between humid and dry, and between alive and dead, mainly due to lack of an appropriate noninvasive technique.

As a promising solution to address this paucity, optical diffraction tomography (ODT) has recently been developed to quantitatively map the mass density distribution inside biological specimens (13,14). By using interferometric microscopy, ODT can determine the three-dimensional (3D) refractive index (RI) distribution of the specimen with high spatial resolution (~120 nm). Because RI is roughly isomorphic to electron density, ODT offers an unbiased and label-free view into the structure of living organisms. Moreover, this structure directly translates into quantitative mass density distributions, because RI and density of materials present in biological samples are linearly proportional (15,16). Although ODT has been extensively used for characterizing the mass density distribution inside individual cells (17,18), its application on larger tissues and whole organisms has hardly been explored.

Here, we show that ODT can be used for imaging the 3D RI distribution in living *C. elegans* larvae with clearly visible morphological features. Reconstructed RI tomograms allowed us to assess the internal mass density distribution, dry mass, and volume of larvae in the reproductive, diapause, and, most importantly, in desiccated stages. The latter gave a unique opportunity to quantify the physical properties of an intact living organism in a desiccated state. We found that the mass density of *C. elegans* larvae increased on entry into dauer diapause—due to radial volume shrinkage at constant dry mass. Further, the dauer larvae in their anhydrobiotic state exhibited very high RI values ($n \sim 1.5$). This value is comparable to that of glass, and rarely seen in biological objects. The desiccated dauer larvae recovered their original volume in response to rehydration, but with significantly reduced dry mass (~25%) and mass density. We also applied ODT to image several mutants that are sensitive to desiccation. Remarkably, one of them, *lea-1*, showed structural defects in the form of void regions with low mass density. Thus, ODT is able to capture the global as well as detailed local changes of biophysical properties throughout the entire larva. We used this method to quantitatively map the material and structural changes accompanying the anhydrobiotic transition in dauer larvae. Our findings open a door to quantitatively understanding the interdependence of material properties of an organism in relation to growth, diapause and cryptobiotic states.

MATERIALS AND METHODS

C. elegans strains and growth conditions

The Caenorhabditis Genetic Center provided the *C. elegans* strain *daf-2(e1370)* and the *Escherichia coli* strain NA22. The compound mutant strains of *daf-2(e1370)III;lea-1(tag1676)V, tps-2(ok526)II; daf-2(e1370) III; tps-1(ok373)X(daf-2;ddtps)* were generated during our previous studies (6,8).

In order to obtain *daf-2(e1370)* eggs, gravid *daf-2* adults were bleached using worm bleaching solution (1 N NaOH, household bleach [5% solution of sodium hypochlorite]) and the eggs were washed several times to remove carcasses and debris. The *daf-2(e1370)* eggs were incubated in 1X M9 buffer for 10 to 12 h at room temperature with shaking to obtain synchronized hatched L1 larvae. These L1 larvae were plated on NGM agar plates with *E. coli* NA22. Half of the plates were incubated at 15°C for obtaining reproductive larval stages and other half were incubated at 25°C for L2d and dauer larvae (19,20). L2 larvae were collected after 48 h, L3 larvae were collected between 64 and 72 h. L2d were collected between 36 and 46 h, and dauer larvae were collected 72 to 82 h after hatching. Larval stages were constantly monitored, visually confirmed for respective stages (for instance nonfeeding and arrested behavior of dauer larvae), and collected from the plate.

Desiccation of *C. elegans* dauer larvae

Larvae at various stages were collected in distilled water and washed twice with water to remove any debris. For preparing preconditioned and desiccated larvae, a dauer suspension of 5 μL was pipetted onto a coverslip (VWR International) and exposed to 98% RH for 4 days and 60% RH for 1 day subsequently. For imaging desiccated dauer larvae, the dauer larvae were immersed in glycerol ($n = 1.4527$) in order to reduce the RI difference between dauer larvae and the surrounding medium. The RI of the medium was measured using an Abbe refractometer (2WAJ; Arcarda GmbH). For imaging rehydrated larvae after desiccation, the dauer larvae were rehydrated for 2 h with water and then anesthetized with levamisole (Sigma) before imaging.

Optical setup for ODT

The 3D RI distribution of *C. elegans* larvae was determined using ODT. The optical setup was described previously (21). Briefly, ODT uses Mach-Zehnder interferometry to measure multiple complex optical fields from various incident angles (Fig. 1 *a*). A laser beam ($\lambda = 532$ nm, frequency-doubled Nd-YAG laser, Torus; Laser Quantum Inc.) was coupled into an optical fiber and divided into two paths using a 2×2 single-mode fiberoptic coupler (TW560R2F2; Thorlabs). One beam was used as a reference beam and the other beam passed through a tube lens ($f = 175$ mm) and a water-dipping objective lens (NA = 1.0, 40×; Carl Zeiss AG) to illuminate the sample on the stage of a home-built inverted microscope. The beam diffracted by the sample was collected with a high numerical-aperture objective lens (NA = 1.2, 63×, water immersion; Carl Zeiss AG) and a tube lens ($f = 200$ mm). To reconstruct a 3D RI tomogram of the sample, the sample was illuminated from 150 different incident angles scanned by a dual-axis Galvano-mirror (GVS012/M; Thorlabs Inc.) located in the conjugate plane of the sample. The diffracted beam interfered with the reference beam at an image plane, and generated a spatially modulated hologram, which was recorded with a charge-coupled device camera (FL3-U3-13Y3M-C, FLIR Systems, Inc.). The total magnification of the setup was 57×, and the field-of-view (FOV) of the camera covers 86.2 μm × 86.2 μm.

Tomogram reconstruction and quantitative analysis

The complex optical fields of light scattered by the samples were retrieved from the recorded holograms by applying a Fourier transform-based field retrieval algorithm (22). To measure the 3D RI tomograms of whole larvae and desiccated dauers, whose size is much larger than the FOV, segmented complex optical fields of the samples were measured and digitally stitched by a custom-made MATLAB script. The 3D RI distribution of the samples was reconstructed from the retrieved complex optical fields via the Fourier diffraction theorem, using the first-order Rytov approximation (13,23). The spatial resolution of RI tomograms in the present study is ∼120 nm (lateral) and ∼440 nm (axial), which are determined by the NAs of the objective lens and condenser lens (24). A more detailed description of tomogram reconstruction can be found elsewhere (25).

On the reconstructed tomograms, Otsu's thresholding method (26) was used to segment the region occupied by the larvae from the background, and quantitative analysis was performed to calculate mean RI value, dry mass, volume, and the standard deviation of RI in the individual larvae. The mass density of the larvae was directly calculated from the mean RI value, since the RI value in biological samples, $n(x,y,z)$, is linearly proportional to the mass density of the material, $\rho(x,y,z)$, as $n(x,y,z) = n_m + \alpha\rho(x,y,z)$, where n_m is the RI value of the surrounding medium and α is the RI increment (dn/dc) with $\alpha = 0.190$ mL/g for proteins and nucleic acids (27,28). The RI of the medium was measured using an Abbe refractometer (2WAJ; Arcarda GmbH). The volume of the larvae was extracted by counting the number of voxels in the segmented region and the dry mass of the larvae was calculated by integrating the mass density inside the segmented region. All tomogram acquisition and data analyses were performed using custom-written MATLAB scripts (R2018b; MathWorks, Inc.), which are available on request. Tomogram rendering was performed by an open-source software (tomviz 1.9.0, https://tomviz.org/). The RI tomograms of all larvae presented in the current study are available from figshare under the following link: https://doi.org/10.6084/m9.figshare.14483331.

Electron microscopy of desiccated dauer larvae

daf-2 and *daf-2; lea-1* dauers that were non-preconditioned, preconditioned (98% RH) and desiccated (60% RH) were rehydrated with a droplet of

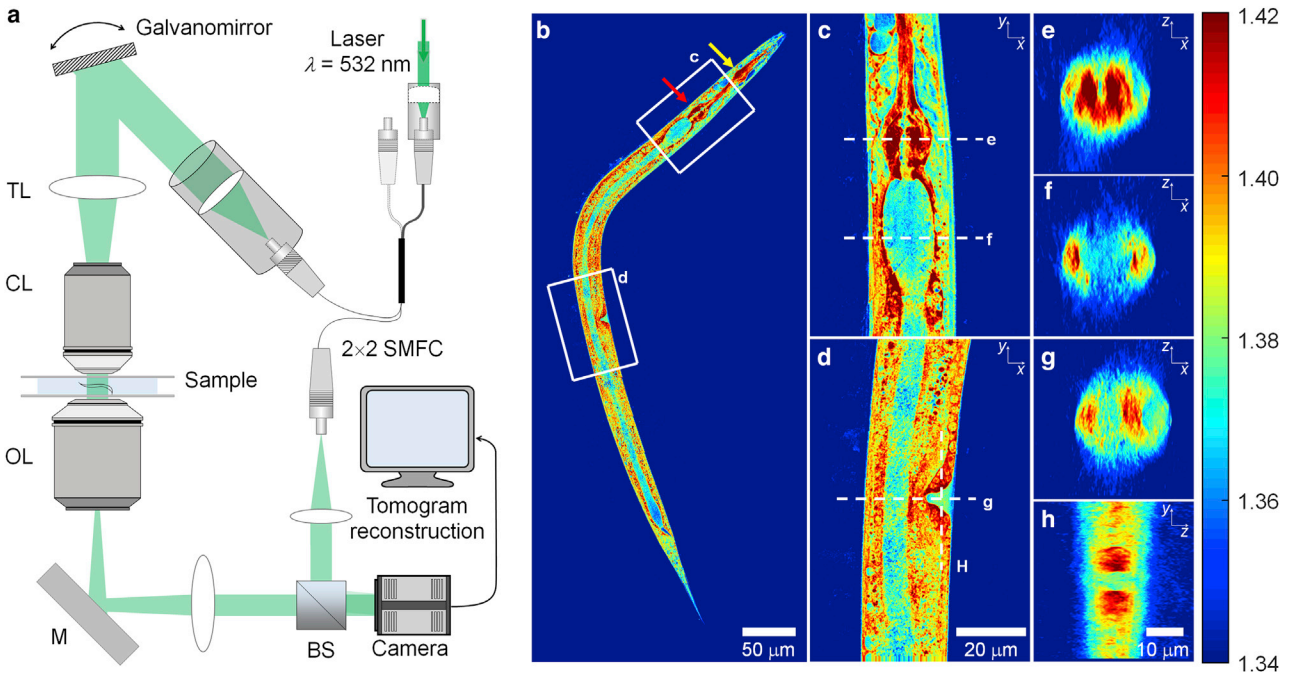

FIGURE 1 Experimental setup and representative 3D RI tomogram of a *C. elegans* larva. (*a*) The setup for ODT. SMFC, single-mode fiber coupler; TL, tube lens; CL, condenser lens; OL, objective lens; M, mirror; and BS, beam splitter. (*b*) Central cross-sectional slice through a 3D RI tomogram along the *x-y* plane of a larva at the L3 stage, and (*c* and *d*) the enlarged cross-sectional RI slices of the pharynx and vulva region indicated in (*b*). *Yellow* and *red arrows* in (*b*) indicate metacorpus and terminal bulb, respectively. (*e* and *f*) Cross-sectional RI slices of (*e*) pharynx and (*f*) gut lumen along the *x-z* plane indicated in (*c*). (*g* and *h*) Cross-sectional RI slices of the vulva region along (*g*) the *x-z* plane and (*h*) *y-z* plane indicated in (*d*). Color scale shows RI. To see this figure in color, go online.

distilled water for 20 min, after which water was soaked off from a corner of the droplet with Kimwipes and bovine serum albumin solution was added. These dauer samples were then transferred to carriers of 3 mm diameter and 0.1 mm depth and rapidly frozen in a high-pressure freezing machine (Leica, EM ICE). For automated freeze substitution, frozen samples from the above step were transferred into vials containing a special freeze substitution cocktail (Acetone, 1% Osmium tetroxide, 0.1% Uranyl acetate) by increasing the temperature to 4.5°C. After thawing, samples were rinsed with acetone to remove any freeze substitution cocktail. Then the samples were infiltrated with Epon LX112 resin:Acetone solution (1:2, 1:1, 2:3) for 1.15 h, 1.30 h, and 2 h, respectively. Finally, they were left in pure resin overnight and then for 4 h. After polymerization and embedding, sections of 70 nm thickness were taken with an ultramicrotome (Leica, UCT) and these sections were incubated in 1% Uranyl acetate in 70% methanol for 10 min, followed by several washes in 70% methanol, 50% methanol, 30% methanol, and finally with distilled water. Sections were further incubated in lead citrate for 5 min, followed by washes with distilled water. Sample sections were analyzed with an electron microscope (Tecnai12; Philips) and images were acquired with a TVIPS camera (Tietz).

Lipid droplet staining and imaging

daf-2(e1370) eggs were plated on NGM agar plates with *E. coli* NA22 mixed with Nile Red (Thermo Scientific, 200 μg/mL). These plates were incubated at 25°C for dauer formation. After 3 days, dauer formation was visually confirmed. Dauer larvae were collected from the plates, and washed thrice with water at 1500 g for 1 min to remove any debris and excess dye adhering to the larvae. The dauer larvae were anesthetized with levamisole (Sigma) and imaged.

Fluorescence emission intensity of Nile Red-stained dauer larvae was measured by epi-fluorescence microscopy combined in the same optical setup as ODT. The detailed configuration is described elsewhere (29). The incoherent light from a halogen lamp (DC-950; Dolan-Jenner Industries Inc.) was passed through a bandpass filter (bandwidth $\lambda = 545 \pm 25$ nm; Carl Zeiss AG), and coupled into the same beam path in the ODT using a three-channel dichroic mirror (FF409/493/596-Di01-25×36; Semrock Inc.). The fluorescence emission signal from Nile Red in lipid droplets was collected by the same objective lens and acquired using the ODT camera. A bandpass filter (bandwidth $\lambda = 605 \pm 70$ nm; Carl Zeiss AG) was placed in front of the camera to suppress the excitation beam. The lipid regions were segmented from measured epi-fluorescence images by applying Otsu's thresholding method and correlated with the cross-sectional slices of RI tomograms, from which the mean RI values of lipid and nonlipid regions were calculated.

Statistical analysis

Measured quantities were reported as mean ± standard error of mean throughout. Statistical significance was determined using Mann-Whitney *U* test. The shown asterisks indicate the statistical significance as *p < 0.01, **p < 0.001, and ***p < 0.0001, respectively.

RESULTS

Quantitative RI and mass density imaging of *C. elegans* larvae

We used ODT, employing Mach-Zehnder interferometric microscopy (Fig. 1 *a*, see materials and methods) to image the spatial distribution of RI inside living *C. elegans* larvae. ODT reconstructed the 3D RI distribution of the specimen with a high spatial resolution of ∼120 nm (lateral) and ∼440 nm (axial) from 2D quantitative phase images obtained from various incident angles. The whole-organism tomogram was enabled by stitching together RI tomograms of multiple FOVs. The mass density was directly calculated from the reconstructed RI tomograms since the RI of most biological samples, n_{sample}, is linearly proportional to the mass density, ρ, as $n_{sample} = n_m + \alpha\rho$, where n_m is the RI of medium and α is the RI increment (*dn/dc*) with $\alpha = 0.190$ mL/g for proteins and nucleic acids (27,28).

Representative high-resolution images of RI tomograms of a larva at the L3 stage, shown in Fig. 1 *b–h* and Video S1, show that ODT can reveal various morphological structures in the RI contrast. Very clearly distinguishable are pharynx (with metacorpus and terminal bulb) and gut (Fig. 1 *c*, *e*, and *f*). Cells of the latter contain lipid droplets with very high RI, whereas the gut lumen exhibits a much lower RI. Interestingly, the pharynx is a tube formed by very tightly packed muscles, and has a similar RI value to that of lipid droplets. In addition, the vulva, having muscles, exhibits a higher RI than the surrounding tissue (Fig. 1 *d*, *g*, and *h*).

Next, we set out to investigate the material properties of different larval stages of *C. elegans* using ODT. For this we took advantage of the *daf-2(e1370)* strain, which enters the reproductive life cycle (L2, L3 larvae) when exposed to 15°C, but which forms dauer larvae at 25°C via an L2d intermediate (19) (Fig. 2 *a* and *b*). The larvae of *daf-2(e1370)* and N2 (wild-type) strain show similar biochemistry and exhibit cryptobiotic, anhydrobiotic survival ability (6,8). We began with larvae at reproductive larval stages (L1, L2, and L3). The representative RI tomograms in Fig. 2 *a* clearly show detailed morphological structures in the larvae. The tomograms also show that the larvae grow in size during the reproductive cycle while maintaining a similar RI value throughout.

By quantitative analysis of the reconstructed tomograms, we characterized length, dry mass, and mean RI value of the larvae (see materials and methods). As expected, both length and dry mass increased during growth from L1 to L3 (Fig. 2 *c* and *d*). Importantly, however, the mean RI value and therefore the mean mass density of the larvae did not change significantly (1.3845 ± 0.0020, 1.3812 ± 0.0024, and 1.3835 ± 0.0032 at L1, L2, and L3 stage, respectively; corresponding to the mass density of 249.8 ± 10.4 mg/mL, 232.4 ± 12.7 mg/mL, and 244.9 ± 16.6 mg/mL; Fig. 2 *e*). These measurements indicate the presence of regulatory mechanisms coordinating the biosynthesis of different classes of molecules required for growth and maintenance of metabolism and structure of cells. Moreover, the standard deviation of RI inside individual larvae at the L1 stage was as low as 0.0120 ± 0.0007 and increased to 0.0164 ± 0.0005 and 0.0165 ± 0.0006 at the L2 and L3 stages, respectively (Fig. 2 *f*). The increasing heterogeneity of RI and mass density quantifies the developmental growth and maturation of organs such as pharynx (with metacorpus and terminal bulb) and gut.

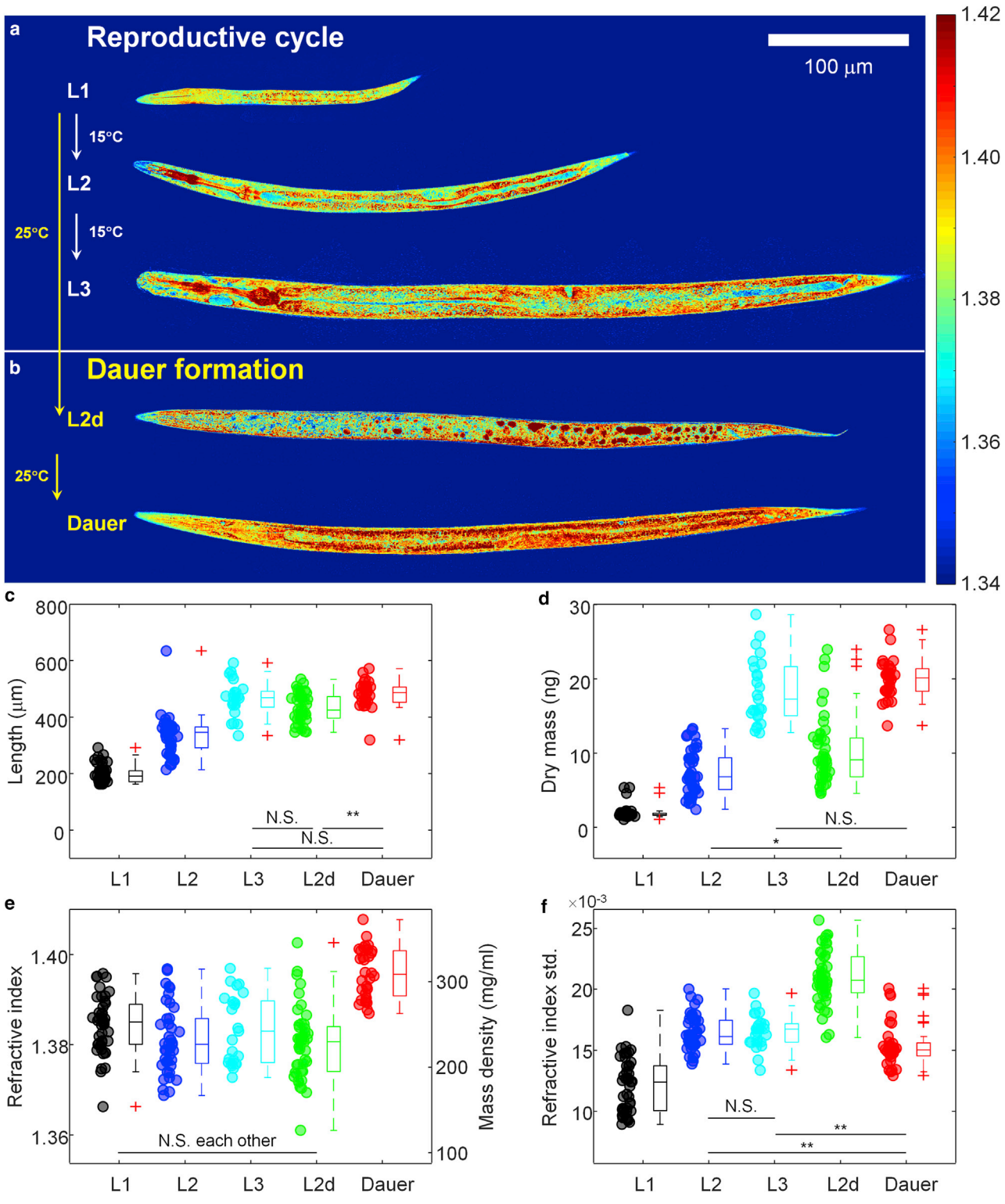

FIGURE 2 Quantitative physical analysis of *C. elegans* larvae at different larval stages. (*a*) Representative central cross-sectional slices through RI tomograms of *C. elegans* larvae at L1, L2, and L3 larval stages in the reproductive cycle. (*b*) Cross-sectional slices through RI tomograms of *C. elegans* larvae at the L2d and dauer stages. Color scale shows RI. (*c–f*) The length (*c*), dry mass (*d*), mean RI and mass density (*e*), and standard deviation of RI (*f*) of *C. elegans* larvae at different larval stages. The numbers of larvae measured are n = 43, 40, 25, 45, and 32 for L1, L2, L3, L2d, and dauer, respectively. The shown asterisks indicate the statistical significance as *$p < 0.01$ and **$p < 0.001$. To see this figure in color, go online.

Dauer larvae have higher mass density than larvae in the reproductive cycle

As a next step, we investigated the RI distribution during the transition into diapause. As shown in Fig. 2 *b* and *e*, the predauer larval stage, called L2d larvae, exhibited a similar average RI value (1.3802 ± 0.0024) to that of larvae in the reproductive cycle. However, the dauer larvae showed significantly higher RI values (1.3960 ± 0.0020). The increased RI, and mass density, of the dauer larvae might correlate with both radial shrinkage and increased accumulation of lipid droplets, known to occur during the transition to diapause (7,19,20,30). We estimated to which extent the accumulation of lipid droplets contributes to the increase in RI and mass density. For this, we correlated the RI tomograms with epi-fluorescence images of dauer larvae stained with Nile Red for lipid droplets in the same optical setup (see materials and methods, Fig. S1 *a* and *b*). The mean RI value of the regions containing lipid droplets was 1.4184 ± 0.0025, which is higher than nonlipid regions with 1.4081 ± 0.0010 (Fig. S1 *c*). In addition, the mean RI value of nonlipid regions by itself was already significantly higher than that of the L3 larvae in the reproductive cycle. Altogether our findings suggest that the increased RI in the dauer larva originates from both volume shrinkage and lipid droplet accumulation. The first increases the overall RI and mass density, whereas the latter contributes to the additional RI increase.

Entry into anhydrobiotic state increases RI and mass density of dauer larvae dramatically

The most interesting findings were revealed in the investigation of morphological and biophysical changes in dauer larvae in a desiccated state. As previously described (6), dauer larvae need to be preconditioned (mild desiccation at 98% RH) to survive harsh desiccation (60% RH; see Fig. 3 *a*). In the process, the larvae lose up to 80% and more than 95% of their body water, respectively. As shown in Fig. 3 *b* and *d*, after desiccation, the RI of dauer larvae displayed surprisingly high RI values: after preconditioning the mean RI was 1.4955 ± 0.0043 and after harsh desiccation 1.4899 ± 0.0028, respectively (Fig. 3 *e*). The increase in RI was so high that to reduce the mismatch between the larvae and the surrounding medium, we immersed the desiccated larvae into glycerol as an imaging medium ($n = 1.4527$). The significant increase of the mean RI in the desiccated dauer larvae was mainly due to the about 2.3- to 2.4-fold decrease in volume (Fig. 3 *f*). In contrast, the dry mass of the dauer larvae decreased only slightly from 17.1 ± 0.9 ng to 16.1 ± 1.2 ng and 15.2 ± 1.3 ng (Fig. 3 *g*).

Most cells and tissues display RI values ranging from 1.35 to 1.39 (31). Reported exceptions are diatoms whose cell walls are made of silica glass that has a high RI value of 1.46 and the basalia spicules of some glass sponges, which can reach RI values of 1.48 in their core (32,33). Remarkably, desiccated dauer larvae had an average RI of almost 1.50 (Fig. 3 *d*), with some internal regions reaching 1.52 (Fig. 3 *c* and *d*), considerably higher than anything reported for other live biological specimens (Fig. S2). Thus, desiccated larvae have optical properties similar to those of dried proteins in vitro or glass, and quite unlike living matter. This, together with the transition of the cytoplasm from a liquid to a solid-like state (due to loss of 95% of body water), seems to be a physical measure of the fact that desiccated *C. elegans* larvae are indistinguishable from inanimate objects.

Upon rehydration with water, the desiccated dauer larvae can revive within a few hours (6) and can develop further into reproductive adults under optimum conditions. As desiccation followed by rehydration induces breakdown of several biomolecules (e.g., triacylglycerols and trehalose) (6,9), we hypothesized that the rehydrated dauer larvae might have different RI values and dry mass in comparison with the dauer larvae before desiccation. As shown in Fig. 4 *a* and *b*, for typical RI tomograms, and Fig. 4 *c*, for quantitative results, the rehydrated dauer larvae had a mean RI value of 1.3971 ± 0.0022, which was significantly lower than that of the dauer larvae before desiccation with 1.4150 ± 0.0013. The rehydrated dauer larvae recovered the volume of dauers before desiccation (53.0 ± 2.2 pL and 55.5 ± 3.3 pL, respectively; Fig. 4 *d*). Interestingly, the dry mass of the dauer larvae decreased by almost 25% from 20.4 ± 0.6 ng before desiccation to 16.1 ± 0.8 ng after rehydration (Fig. 4 *e*). This result quantitatively confirms our previous findings that the dauer larvae consume significant amounts of triacylglycerols and trehalose during desiccation and rehydration—they metabolize a quarter of their own internal contents in the process.

ODT reveals structural differences in desiccation-sensitive mutants

Previous studies have shown that *C. elegans* dauer larvae activate several biochemical pathways to survive harsh desiccation (10). One of them leads to massive biosynthesis of the disaccharide trehalose, which is involved in protecting phospholipid bilayers against water-induced damage during rehydration (6). Another essential factor for survival is biosynthesis of an intrinsically disordered protein LEA-1 (late embryogenesis abundant) (8,10). Deletion mutants with the biosynthetic pathways of trehalose (double mutant lacking biosynthetic enzymes TPS-1 and TPS-2, *daf-2;ΔΔtps*) or of LEA-1 (*daf-2;lea-1*) abolished are nonviable after rehydration (8). Thus, we investigated how deficiency in trehalose and LEA-1 in these mutants influences the physical characteristics of desiccated dauer larvae. Is there a correlation between the latter and the viability of larvae?

As shown in Fig. 5 and Videos S2, S3, and S4 for the representative ODTs, and Fig. S3 *a* for the quantitative

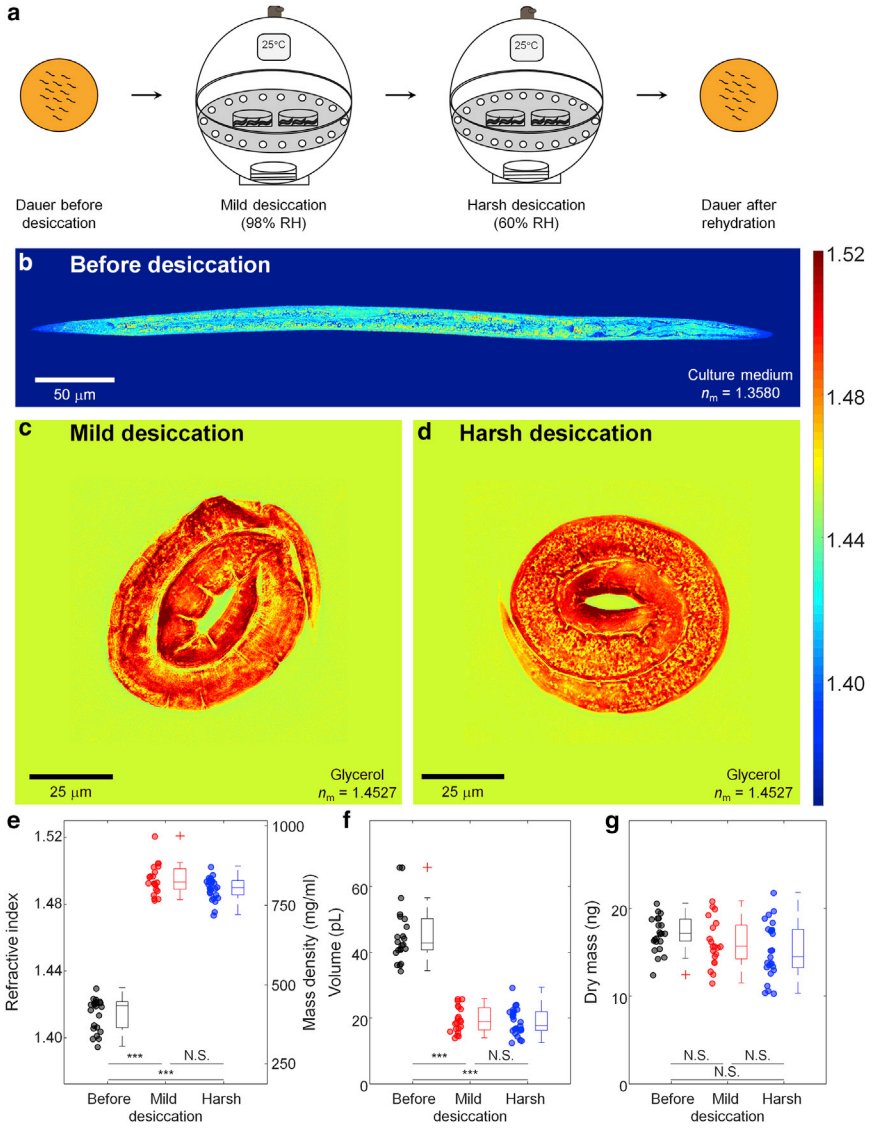

FIGURE 3 Quantitative ODT analysis of desiccated dauer larvae. (*a*) Schematic diagram for preparing *C. elegans* dauer larvae by consecutive mild (98% RH) and harsh desiccation (60% RH). (*b*) Central cross-sectional slice through RI tomogram of a typical *C. elegans* dauer larva (similar to Fig. 2 *b*, but with different RI scale). (*c* and *d*) Representative cross-sectional slices through RI tomograms of desiccated dauer larvae after (*c*) mild (98% RH) and (*d*) harsh (60% RH) desiccation. Color scale shows RI. (*e–g*) Mean RI (*e*), volume (*f*), and dry mass (*g*) of *C. elegans* dauer larvae in different desiccated stages. The numbers of desiccated larvae measured are n = 22, 20, and 25 for dauer, mild, and harsh desiccated state, respectively. The shown asterisks indicate the statistical significance as ***$p < 0.0001$. To see this figure in color, go online.

analysis, the trehalose and LEA-1 deletions did not affect overall mean RI value and mass density significantly—neither before nor after mild and harsh desiccation. Only the dauer larvae of the *lea-1* deletion mutant had a slightly lower mean RI value than wild-type dauer larvae. Not surprising for mutants that cannot produce trehalose, the volume and dry mass of the dauer larvae before and during desiccation were lower than that of control dauer larvae in the same conditions (Figs. 5 *d–f*, S3 *b* and *c*). The result is consistent with previous studies showing that trehalose is produced largely during the preconditioning (6). However, since volume and mass changes in the trehalose mutants scaled proportionally, the overall densities of wild-type and both mutant larvae were similar in the anhydrobiotic state.

Even though the *lea-1* mutants were inconspicuous in their overall physical properties, they displayed very interesting internal structural anomalies. As seen in Fig. 5 *h* and *i*, the RI tomograms of desiccated dauer larvae of the *lea-1* deletion mutant displayed distinct void regions with significantly lower RI value. By visual inspection, the void regions corresponded to mid-gut regions anatomically. This finding, based on ODT measurements, quantifies morphological and physicochemical differences in desiccated samples that are hardly, or not at all revealed by light or electron microscopy (EM). As seen in Fig. S4, bright field microscopy did not display any difference in contrast to wild-type. Differential interference contrast microscopy did show circular structures that might correspond to the void volumes detected by ODT, but without the 3D imaging and quantification capabilities of ODT, one cannot determine these differences in local material properties with certainty. Further, imaging with ODT has considerable advantages to EM stemming from the fact that it can image specimens in their native state and without any preparative steps, as in EM, that are necessarily destructive and also

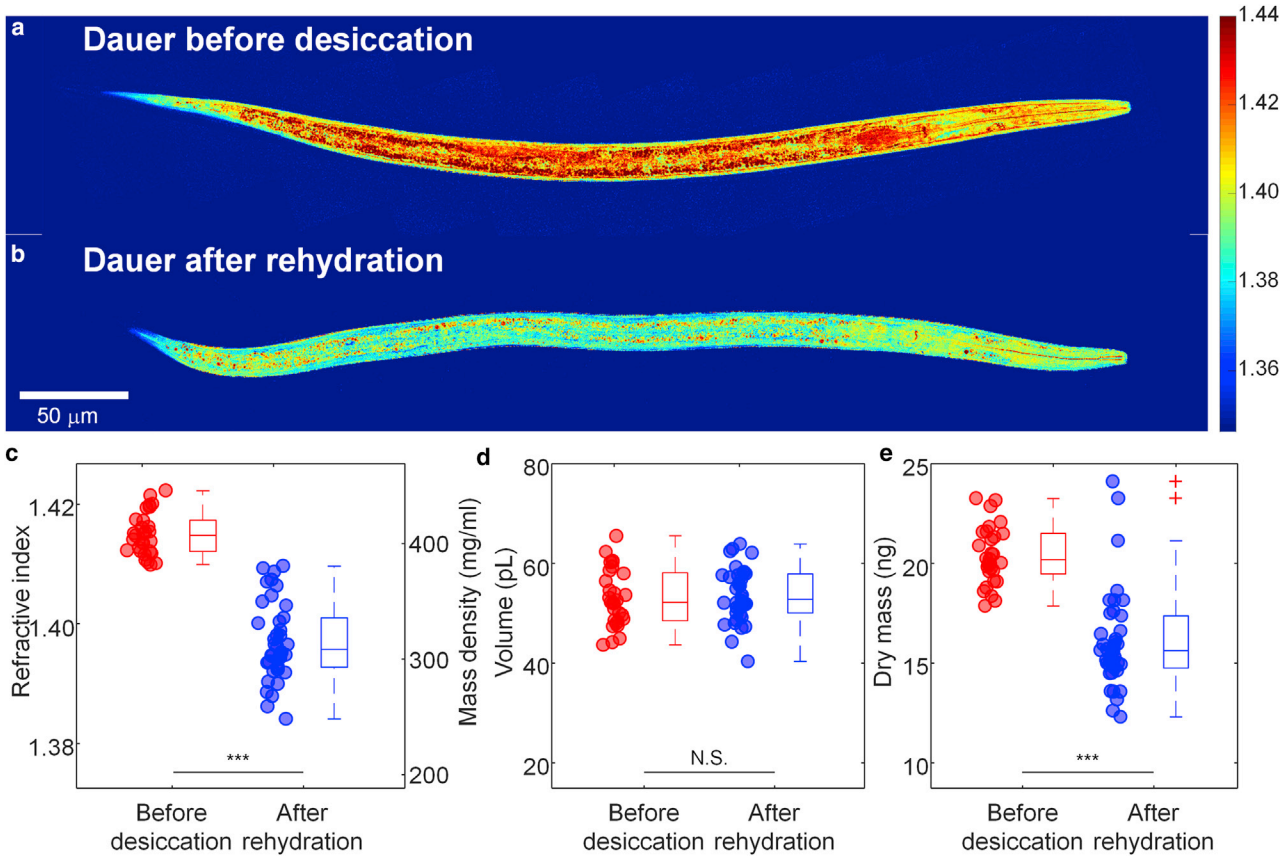

FIGURE 4 Quantitative ODT analysis of dauer larvae before desiccation and after rehydration. (*a* and *b*) Central cross-sectional slices of RI tomograms of typical *C. elegans* dauer larvae (*a*) before desiccation and (*b*) after rehydration. Color scale shows RI. (*c–e*) Mean RI and mass density (*d*) and dry mass (*e*) of *C. elegans* dauer larvae before desiccation and after rehydration. The numbers of dauer larvae measured are n = 29 and 38, respectively. The shown asterisks indicate the statistical significance as ***$p < 0.0001$. To see this figure in color, go online.

bear the danger of creating artifacts or eliminating differences. It must be said that EM principally does not allow the analysis of a desiccated *C. elegans* dauer larva, as it can only be applied to samples after partial rehydration. The electron micrographs of the dauer larvae of *lea-1* deletion mutant after harsh desiccation, and subsequently necessary rehydration, show that the annular morphology of the desiccated larvae is distorted (Fig. S5). This observation can, however, only indirectly indicate possible structural changes of *lea-1* dauer larvae in the desiccated state.

The measured RI tomograms were further analyzed quantitatively to investigate the mass density difference in void regions. The void regions were segmented from the RI tomograms by applying the Otsu method (26), and the mean RI value of the void regions and peripheral regions was quantified. The periphery of the void regions was segmented by dilating the binary masks for the void regions by 5 μm. The mean RI value of the void regions of the dauer larvae in mild and harsh desiccation conditions was 1.4686 ± 0.0004 and 1.4686 ± 0.0006, respectively, which were significantly lower than the peripheral regions with 1.4962 ± 0.0006 and 1.4972 ± 0.0008 (Fig. S6). The relative RI difference suggests that the void region is 18% less dense than peripheral regions. Altogether our ODT-based findings shed light onto the quantitative correlation between material and structural properties of an organism and its survival ability in extreme environments.

DISCUSSION

In this study, we used ODT to reconstruct the 3D RI distribution of *C. elegans* larvae in reproductive stages and dauer diapause. From these RI tomograms, the physical properties, including mass density, volume, and dry mass were quantitatively analyzed. So far, ODT has mostly been applied for single-cell analysis mainly due to the limited FOV (17,18), and few studies briefly visualized the RI tomograms of *C. elegans* (34,35). This study is the first quantitative ODT analysis of an entire organism.

We used ODT to provide the biophysical and structural properties of live dauer larvae, which have not been charted by conventional microscopic techniques. Previously, EM had been used to reveal the fine structures of dauer larvae and their density differences under harsh desiccation

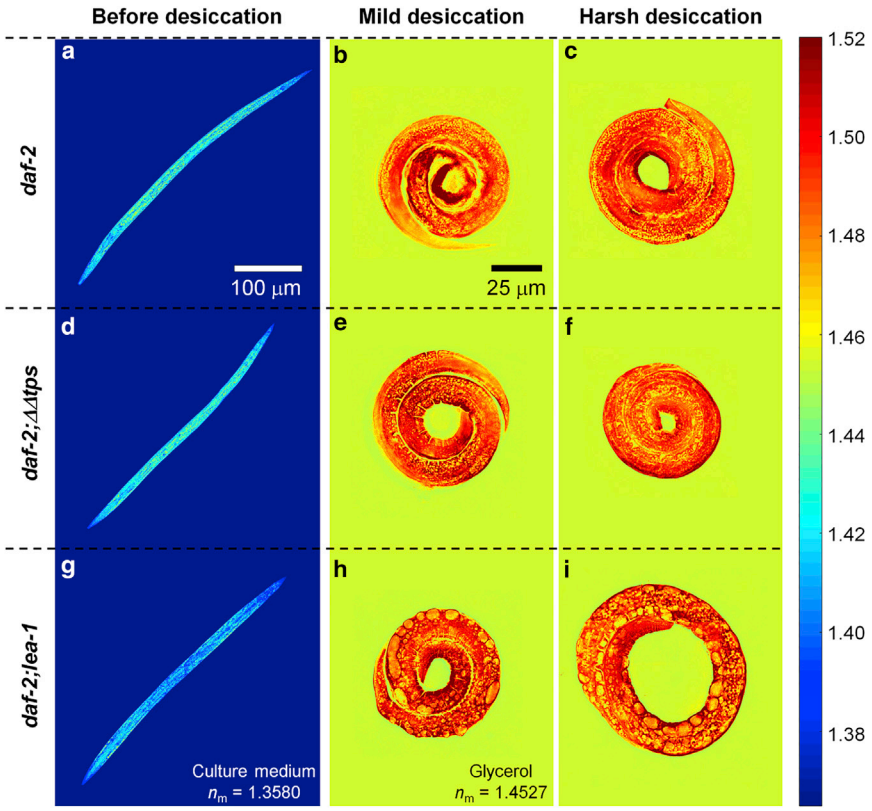

FIGURE 5 ODT analysis of desiccated dauer larvae with different genetic mutations. Typical central cross-sectional slices through RI tomograms of *C. elegans* dauer larvae of (*a–c*) controls, (*d–f*) trehalose deletion mutants *daf-2;ΔΔtps*, and (*g–i*) *lea-1* deletion mutants *daf-2;lea-1*, respectively. (*a*, *d*, *g*) represent dauer larvae before, (*b*, *e*, *h*) after mild (98% RH), and (*c*, *f*, *i*) after harsh desiccation (60% RH). Color scale shows RI. To see this figure in color, go online.

conditions with its typical very high spatial resolution (6,20). However, the sample preparation for desiccated dauer larvae requires rehydrating the larvae for a brief time before further processing. Thus, EM images we obtain do not depict larvae in a desiccated state but rather depict changes that occur after first desiccation and then subsequent rehydration. ODT might not provide the same spatial resolution as EM, but it can quantitatively assess structure and physical properties of intact dauer larvae without any sample preparation steps. In principle, ODT can even trace the changes within the same larvae during development and the desiccation process. As another relevant light microscopy, fluorescence microscopy provides molecularly specific localization of fluorescently stained proteins and organelles in live dauer larvae; however, fluorescence imaging is susceptible to phototoxicity and can only visualize molecules labeled selectively. It is not suitable to quantify physical properties and their changes. In contrast, ODT allows revealing the mass density of overall unbiased substances in the entire organism. Because *C. elegans* larvae can be considered optically transparent, at least up to the L3 stage in the reproductive life cycle (36), the first-order Rytov approximation is still valid for reconstructing RI tomograms. To extend analysis to even larger and optically denser specimens, various computational algorithms for tomogram reconstruction have recently been developed to take into account multiple photon scattering in the sample (35,37). Using such algorithms, we can extend our studies in the future also to L4 larvae and adult *C. elegans* worms.

From reconstructed RI tomograms, we found that the *C. elegans* larvae in the reproductive cycle maintain a constant mass density during development, while entry to dauer diapause increases the mass density significantly. From the correlation between the RI tomograms and epi-fluorescence images of Nile Red-stained lipid droplets, we conclude that the increased mass density in dauer larvae is presumably due to this lipid droplet accumulation, in addition to the radial shrinkage they undergo during dauer formation. This hypothesis can be tested by analyzing whether mutant strains that do not undergo proper radial shrinkage (19,20) or that deplete lipid droplets rapidly (38) exhibit a similar increase in mass density.

Biophysical properties of organisms that can survive extreme environments have until now only sporadically been studied in some models such as tardigrades and cells (39,40). One remarkable finding of our study is that dauer larvae in their anhydrobiotic state (where most of the body water is lost) have a very high RI value reaching $n \sim 1.5$. This RI value is usually not found in live biological specimens and is comparable to that of dried proteins in vitro or glass (Fig. S2). Although this finding needs further investigation into the biological relevance of why and how desiccated dauer larvae acquire such high RI and mass density, one can speculate that the increased mass

density may reflect a glass transition of the cytoplasm during desiccation, which has been reported in cells with high mass density and in desiccated tardigrades (39,40). It is conceivable that such a transition contributes to an increased mechanical stability in the desiccated state of the organism. This hypothesis needs further validation by direct measurements of mechanical properties of desiccated dauer larvae, such as differential scanning calorimetry or conventional, contact-based techniques for mechanical phenotyping, such as atomic force microscopy-enabled nanoindentation (41). Furthermore, noninvasive microscopic techniques have recently emerged to probe the mechanical properties of biological samples directly inside living biological samples, including Brillouin microscopy (42–45) and time-lapse quantitative phase microscopy (46,47). Combining ODT with such microscopic techniques can in the future provide decisive information on the detailed nature of the material transitions during dauer formation and desiccation of *C. elegans* larvae.

Our measurements on rehydrated dauer larvae revealed that the dry mass is significantly decreased (~25%) in rehydrated larvae while their volume remains constant. It is worth noting that ODT provides absolute and unbiased quantification of how much material the larvae consume during the rehydration process. In accordance with our previous results, we found that the degradation of essential biomolecules (triacylglycerols, trehalose) upon desiccation and rehydration (6,9) manifest on the dry mass content of the dauer larvae. The significant increase and decrease of mass density during harsh desiccation and rehydration without damage draw our attention to the connection between biochemical pathways and material properties of the larvae in such dramatic transitions. Hence, we quantitatively characterized the physical differences of deletion mutants that do not survive desiccation. To the best of our knowledge, this is the first study reporting the overall changes in the RI and mass density distributions of an entire multicellular organism with genetic mutations. The mean RI value of the deletion mutants remained the same as the wild-type desiccated larvae. However, we observed a decreased dry mass and void regions with low mass density in deletion mutants. The trehalose deletion mutant (*daf-2;ΔΔtps*) displayed a decreased dry mass, which is in accordance with our previous observation that trehalose levels are normally accumulated during desiccation (6). The *lea-1* deletion mutant larvae showed distinct structural differences in the RI distribution during desiccation, as they exhibited void regions with significantly lower RI value in the RI tomograms. The molecular mechanism of how LEA-1 confers desiccation tolerance to dauer larvae remains elusive. Several in vitro studies have indicated that LEA-1 is involved in the prevention of protein aggregation during desiccation (48,49). In combination with our EM results, the structural defects in the RI tomograms of *lea-1* deletion mutant indicate that LEA-1 might maintain the functionality of cytosolic proteins that further assist in the maintenance of the annular morphology of the desiccated larvae (Fig. S4). Further correlative investigations with fluorescently tagged LEA-1 in wild-type larvae and corresponding regions in *lea-1* deletion mutant should lead toward the precise mechanism.

To conclude, we used ODT to quantitatively investigate the physical and structural changes in a living *C. elegans* larva during dauer formation and upon desiccation. We revealed that the RI of dauer larvae is higher than that of larvae in the reproductive cycle, and becomes even as high as the RI of glass ($n \sim 1.5$) in the desiccated state. Moreover, dauer larvae of the deletion mutants of trehalose and LEA-1 exhibited distinct morphological changes in the desiccation condition, which may affect survival in such harsh environments. The biological relevance of a higher mass density of the larvae during dauer formation and upon desiccation requires further investigation. However, the physical understanding and corresponding quantitative modeling of cryptobiotic transitions in *C. elegans* larvae can now be based on actual physical parameters determined by methods such as ODT. As such, our study paves the way to a more complete understanding of the underlying mechanisms to sustain the integrity of nematodes, and ultimately other organisms, in transitions between life and death.

SUPPORTING MATERIAL

Supporting material can be found online at https://doi.org/10.1016/j.bpj.2022.02.031.

AUTHOR CONTRIBUTIONS

K.K. conducted the ODT measurements and analyzed the data; V.G. prepared the *C. elegans* larvae; K.K. and V.G. interpreted the ODT data; K.K., V.G., T.K., and J.G. contributed to the conception and design of the study and interpretation of the results, and wrote the manuscript.

ACKNOWLEDGMENTS

We thank Vasily Zaburdaev, Simon Alberti, Gheorghe Cojoc, Raimund Schlüßler, Titus M. Franzmann, Hui-Shun Kuan, Shada Abuhattum, and Anne Eβlinger for helpful discussions. We thank Daniela Vorkel from the electron microscopy facility of MPI-CBG for technical assistance. The authors acknowledge financial support from the Volkswagen Foundation (Life? research grant 92847).

REFERENCES

1. Young, I. E., and P. C. Fitz-James. 1959. Chemical and morphological studies of bacterial spore formation. *J. Biophys. Biochem. Cytol.* 6:467–482.
2. Cochrane, V. W. 1974. Dormancy in spores of fungi. *Trans. Am. Microsc. Soc.* 93:599.
3. Bewley, J. D. 1997. Seed germination and dormancy. *Plant Cell.* 9:1055–1066.

4. Sommerville, R. I., and K. G. Davey. 2002. Diapause in parasitic nematodes: a review. *Can. J. Zool.* 80:1817–1840.
5. Hibshman, J. D., J. S. Clegg, and B. Goldstein. 2020. Mechanisms of desiccation tolerance: themes and variations in brine shrimp, roundworms, and tardigrades. *Front. Physiol.* 11:592016.
6. Erkut, C., S. Penkov, …, T. V. Kurzchalia. 2011. Trehalose renders the dauer larva of *Caenorhabditis elegans* resistant to extreme desiccation. *Curr. Biol.* 21:1331–1336.
7. Golden, J. W., and D. L. Riddle. 1984. The *Caenorhabditis elegans* dauer larva: developmental effects of pheromone, food, and temperature. *Dev. Biol.* 102:368–378.
8. Gade, V. R., S. Traikov, …, T. V. Kurzchalia. 2020. *C. elegans* possess a general program to enter cryptobiosis that allows dauer larvae to survive different kinds of abiotic stress. *Sci. Rep.* 10:13466.
9. Erkut, C., V. R. Gade, …, T. V. Kurzchalia. 2016. The glyoxylate shunt is essential for desiccation tolerance in *C. elegans* and budding yeast. *Elife.* 5:e13614.
10. Erkut, C., A. Vasilj, …, T. V. Kurzchalia. 2013. Molecular strategies of the *Caenorhabditis elegans* dauer larva to survive extreme desiccation. *PLoS One.* 8:e82473.
11. Shannon, A. J., J. A. Browne, …, A. M. Burnell. 2005. The anhydrobiotic potential and molecular phylogenetics of species and strains of *Panagrolaimus* (Nematoda, Panagrolaimidae). *J. Exp. Biol.* 208: 2433–2445.
12. Perry, R. N., and D. A. Wharton. 2011. Molecular and Physiological Basis of Nematode Survival. CABI.
13. Sung, Y., W. Choi, …, M. S. Feld. 2009. Optical diffraction tomography for high resolution live cell imaging. *Opt. Express.* 17:266–277.
14. Park, Y., C. Depeursinge, and G. Popescu. 2018. Quantitative phase imaging in biomedicine. *Nat. Photon.* 12:578–589.
15. Barer, R. 1952. Interference microscopy and mass determination. *Nature.* 169:366–367.
16. Popescu, G., Y. Park, …, K. Badizadegan. 2008. Optical imaging of cell mass and growth dynamics. *Am. J. Physiol. Physiol.* 295:C538–C544.
17. Kim, K., J. Yoon, …, Y. Park. 2016. Optical diffraction tomography techniques for the study of cell pathophysiology. *J. Biomed. Photon. Eng.* 2:020201.
18. Midtvedt, D., E. Olsén, …, G. D. M. Jeffries. 2019. Label-free spatiotemporal monitoring of cytosolic mass, osmolarity, and volume in living cells. *Nat. Commun.* 10:340.
19. Gems, D., A. J. Sutton, …, D. L. Riddle. 1998. Two pleiotropic classes of *daf-2* mutation affect larval arrest, adult behavior, reproduction and longevity in Caenorhabditis elegans. *Genetics.* 150:129–155.
20. Penkov, S., B. K. Raghuraman, …, T. V. Kurzchalia. 2020. A metabolic switch regulates the transition between growth and diapause in *C. elegans*. *BMC Biol.* 18:31.
21. Abuhattum, S., K. Kim, …, J. Guck. 2018. Intracellular mass density increase is accompanying but not sufficient for stiffening and growth arrest of yeast cells. *Front. Phys.* 6:131.
22. Cuche, E., P. Marquet, and C. Depeursinge. 2000. Spatial filtering for zero-order and twin-image elimination in digital off-axis holography. *Appl. Opt.* 39:4070–4075.
23. Wolf, E. 1969. Three-dimensional structure determination of semitransparent objects from holographic data. *Opt. Commun.* 1:153–156.
24. Lauer, V. 2002. New approach to optical diffraction tomography yielding a vector equation of diffraction tomography and a novel tomographic microscope. *J. Microsc.* 205:165–176.
25. Kim, K., H. Yoon, …, Y. Park. 2014. High-resolution three-dimensional imaging of red blood cells parasitized by *Plasmodium falciparum* and *in situ* hemozoin crystals using optical diffraction tomography. *J. Biomed. Opt.* 19:011005.
26. Otsu, N. 1979. A threshold selection method from gray-level histograms. *IEEE Trans. Syst. Man. Cybern.* 9:62–66.
27. Zhao, H., P. H. Brown, and P. Schuck. 2011. On the distribution of protein refractive index increments. *Biophys. J.* 100:2309–2317.
28. Zangle, T. A., and M. A. Teitell. 2014. Live-cell mass profiling: an emerging approach in quantitative biophysics. *Nat. Methods.* 11: 1221–1228.
29. Kim, K., and J. Guck. 2020. The relative densities of cytoplasm and nuclear compartments are robust against strong perturbation. *Biophys. J.* 119:1946–1957.
30. Matyash, V., E. V Entchev, …, T. V Kurzchalia. 2004. Sterol-derived hormone(s) controls entry into diapause in *Caenorhabditis elegans* by consecutive activation of DAF-12 and DAF-16. *PLoS Biol.* 2:e280.
31. Liu, P. Y., L. K. Chin, …, Y. Leprince-Wang. 2016. Cell refractive index for cell biology and disease diagnosis: past, present and future. *Lab Chip.* 16:634–644.
32. Aizenberg, J., V. C. Sundar, …, G. Chen. 2004. Biological glass fibers: correlation between optical and structural properties. *Proc. Natl. Acad. Sci. U S A.* 101:3358–3363.
33. Soto, J. M., J. A. Rodrigo, and T. Alieva. 2017. Label-free quantitative 3D tomographic imaging for partially coherent light microscopy. *Opt. Express.* 25:15699–15712.
34. Choi, W., C. Fang-Yen, …, M. S. Feld. 2007. Tomographic phase microscopy. *Nat. Methods.* 4:717–719.
35. Chowdhury, S., M. Chen, …, L. Waller. 2019. High-resolution 3D refractive index microscopy of multiple-scattering samples from intensity images. *Optica.* 6:1211–1219.
36. Ntziachristos, V. 2010. Going deeper than microscopy: the optical imaging frontier in biology. *Nat. Methods.* 7:603–614.
37. Lim, J., A. B. Ayoub, …, D. Psaltis. 2019. High-fidelity optical diffraction tomography of multiple scattering samples. *Light Sci. Appl.* 8:82.
38. Narbonne, P., and R. Roy. 2009. *Caenorhabditis elegans* dauers need LKB1/AMPK to ration lipid reserves and ensure long-term survival. *Nature.* 457:210–214.
39. Boothby, T. C., H. Tapia, …, B. Goldstein. 2017. Tardigrades use intrinsically disordered proteins to survive desiccation. *Mol. Cell.* 65:975–984.e5.
40. Nishizawa, K., K. Fujiwara, …, D. Mizuno. 2017. Universal glass-forming behavior of *in vitro* and living cytoplasm. *Sci. Rep.* 7:15143.
41. Möllmert, S., M. A. Kharlamova, …, J. Guck. 2020. Zebrafish spinal cord repair is accompanied by transient tissue stiffening. *Biophys. J.* 118:448–463.
42. Scarcelli, G., W. J. Polacheck, …, S. H. Yun. 2015. Noncontact three-dimensional mapping of intracellular hydromechanical properties by Brillouin microscopy. *Nat. Methods.* 12:1132–1134.
43. Schlüßler, R., S. Möllmert, …, J. Guck. 2018. Mechanical mapping of spinal cord growth and repair in living zebrafish larvae by Brillouin imaging. *Biophys. J.* 115:911–923.
44. Remer, I., R. Shaashoua, …, A. Bilenca. 2020. High-sensitivity and high-specificity biomechanical imaging by stimulated Brillouin scattering microscopy. *Nat. Methods.* 17:913–916.
45. Schlüßler, R., K. Kim, …, J. Guck. 2022. Correlative all-optical quantification of mass density and mechanics of subcellular compartments with fluorescence specificity. *Elife.* 11:e68490.
46. Ma, L., G. Rajshekhar, …, G. Popescu. 2016. Phase correlation imaging of unlabeled cell dynamics. *Sci. Rep.* 6:32702.
47. Drechsler, M., F. Giavazzi, …, I. M. Palacios. 2017. Active diffusion and advection in *Drosophila* oocytes result from the interplay of actin and microtubules. *Nat. Commun.* 8:1520.
48. Chakrabortee, S., C. Boschetti, …, A. Tunnacliffe. 2007. Hydrophilic protein associated with desiccation tolerance exhibits broad protein stabilization function. *Proc. Natl. Acad. Sci. U S A.* 104:18073–18078.
49. Chakrabortee, S., R. Tripathi, …, A. Tunnacliffe. 2012. Intrinsically disordered proteins as molecular shields. *Mol. Biosyst.* 8:210–219.

Biophysical Journal, Volume *121*

Supplemental information

Quantitative imaging of *Caenorhabditis elegans* dauer larvae during cryptobiotic transition

Kyoohyun Kim, Vamshidhar R. Gade, Teymuras V. Kurzchalia, and Jochen Guck

Supplementary Information for

Quantitative imaging of *Caenorhabditis elegans* dauer larvae during cryptobiotic transition

Kyoohyun Kim[1,2,†], Vamshidhar R. Gade[3,4,†], Teymuras V. Kurzchalia[3,*],

and Jochen Guck[1,2,*]

[1]Biotechnology Center, Center for Molecular and Cellular Bioengineering, Technische Universität Dresden, 01307 Dresden, Germany

[2]Max Planck Institute for the Science of Light & Max-Planck-Zentrum für Physik und Medizin, 91058 Erlangen, Germany

[3]Max Planck Institute of Molecular Cell Biology and Genetics, 01307 Dresden, Germany

[4]Present address: Institute of Biochemistry, ETH Zürich, 8093 Zürich, Switzerland

[†]K.K. and V.G. contributed equally to this work.

[*]To whom correspondence may be addressed.

Email: kurzchalia@mpi-cbg.de or jochen.guck@mpl.mpg.de

This PDF file includes:

Figures S1 to S6
Legends for Movies S1 to S4
SI References

Other supplementary materials for this manuscript include the following:

Movies S1 to S4

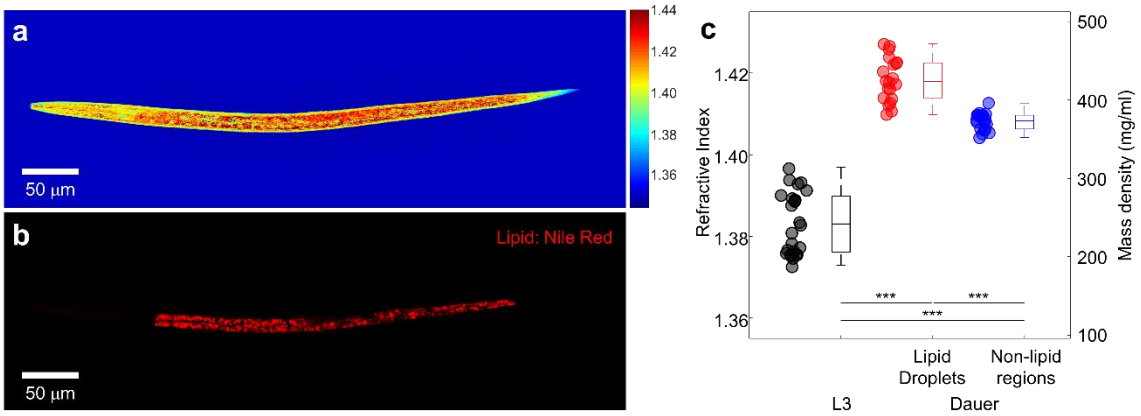

Supplementary Figure 1. Correlation between refractive index (RI) tomograms and epi-fluorescence images of lipid droplets in dauer larvae. (a) Central cross-sectional slice through an RI tomogram of a typical dauer larva. Color scale shows RI. (b) Epi-fluorescence image of the same dauer larva in which the lipid content is stained with Nile Red. (c) Mean RI of larvae at the L3 stage and lipid droplets and non-lipid regions in the Nile Red-stained dauer larvae. The RI distribution of larvae at the L3 stage is reused from Figure 2e. Please note that the absolute values of both lipid droplets and non-lipid regions are slightly higher than the overall RI values reported in Figure 2b and e. This could either be due to a slight batch-to-batch variability in the dauers or to a slight increase in the mass density due to the Nile Red staining. The numbers of L3 and dauer larvae measured are N = 25 and 20, respectively.

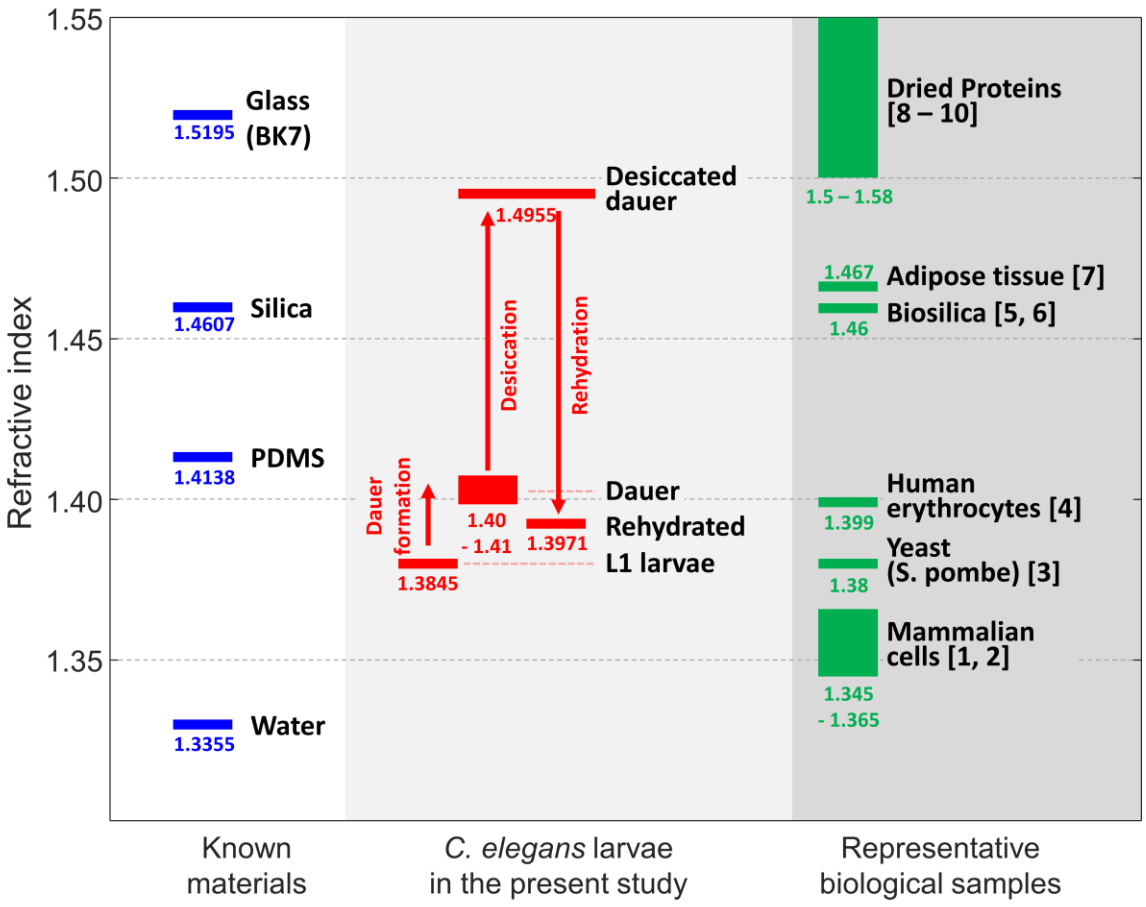

Supplementary Figure 2. Graphical summary on the measured refractive index (RI) value of *C. elegans* larvae in the present study (center) compared to the RI of known inanimate materials (left) and representative biological samples (right).

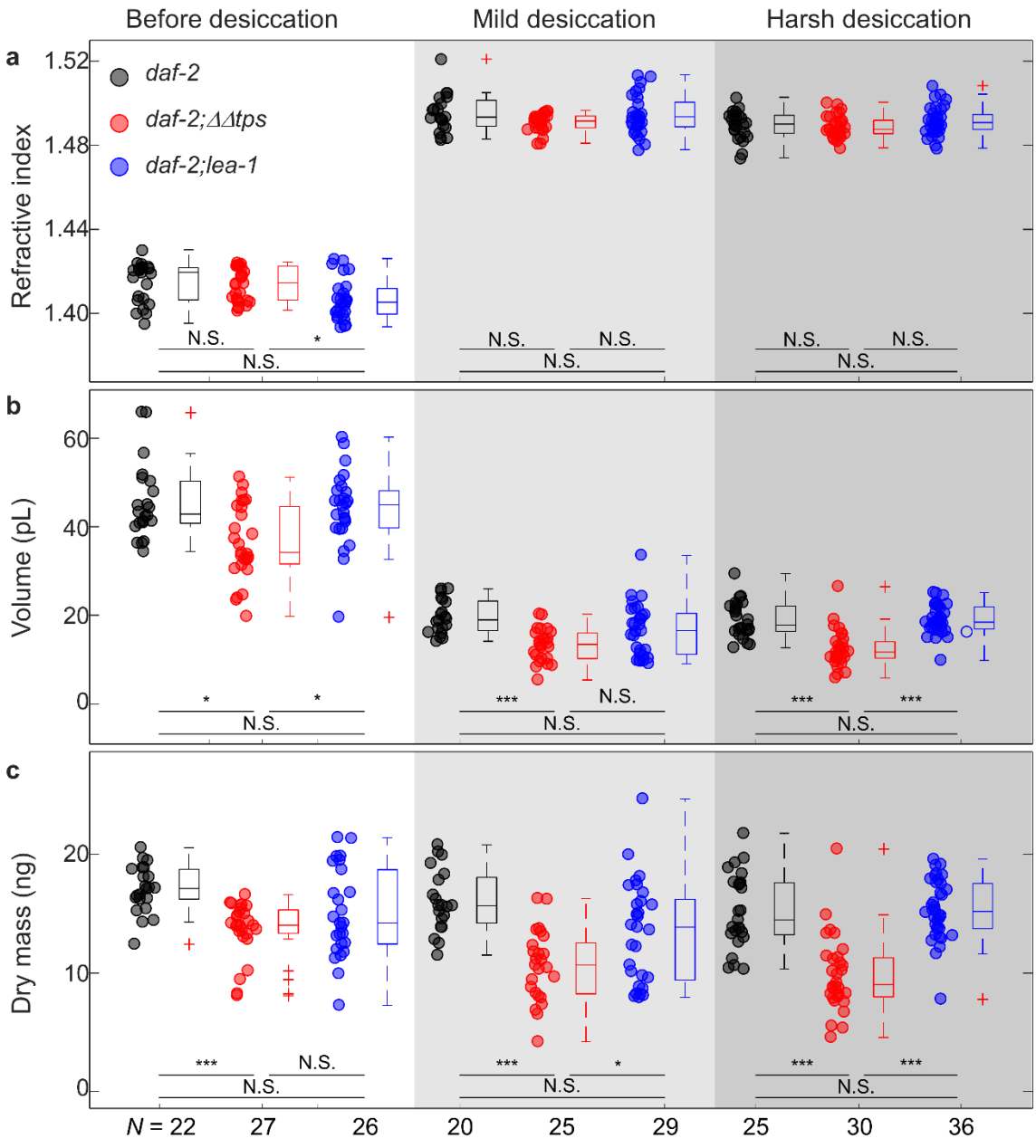

Supplementary Figure 3. Quantitative characterization of wild type (black), trehalose deletion mutant (red), and LEA-1 deletion mutant (blue) dauer larvae in different conditions. (a) The mean refractive index, (b) volume, and (c) dry mass of the dauer larvae.

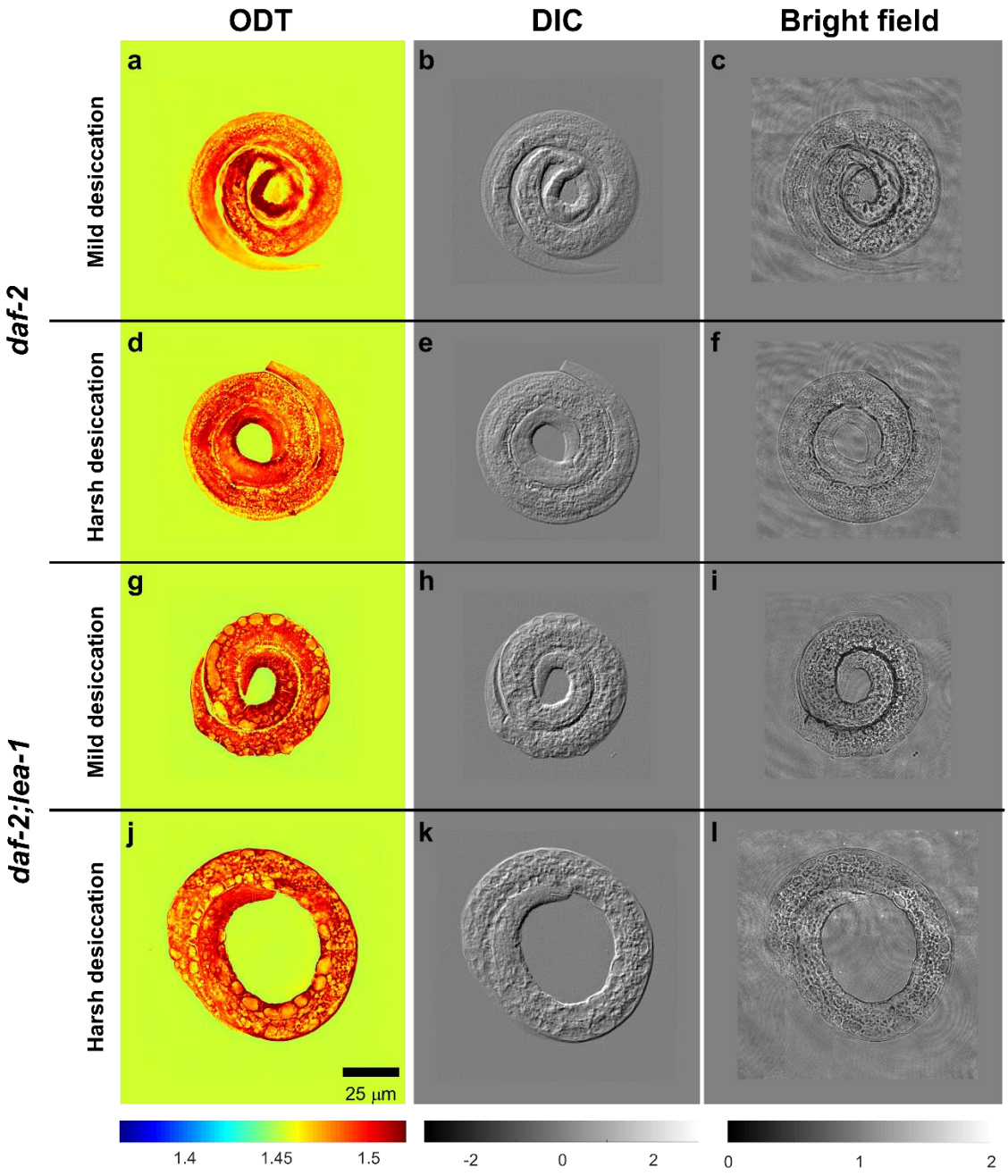

Supplementary Figure 4. Comparison of images acquired by different microscopy modalities. (a, d, g, j) Typical central cross-sectional slices through RI tomograms, (b, e, h, k) emulated differential interference contrast (DIC) images, and (c, f, i, l) bright field images of *C. elegans* dauer larvae. (a – c) represent wild type after mild (98% RH) desiccation, (d – f) wild type after harsh (60% RH) desiccation, (g – i) lea-1 deletion mutants *daf-2;lea-1* after mild desiccation, and (j – l) *daf-2;lea-1* after harsh desiccation. Color scale shows RI. Grey scales show light intensity in the arbitrary unit.

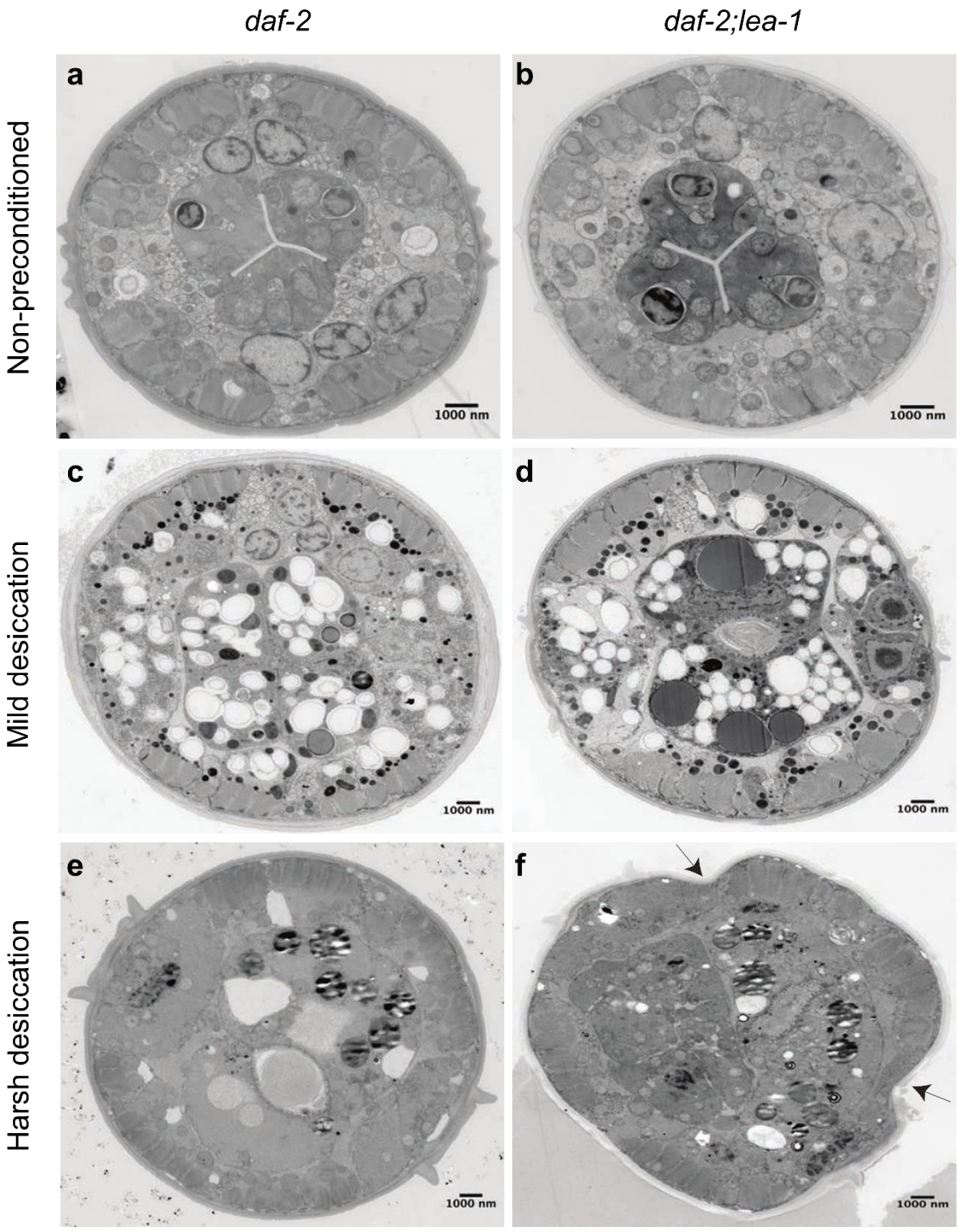

Supplementary Figure 5. Electron micrographs of (a, c, e) wild type (*daf-2*) and (b, d, f) *lea-1* deletion mutant (*daf-2;lea-1*) in (a, b) the non-preconditioned, (c, d) mild desiccation, and (e, f) harsh desiccation conditions. The arrows in f indicate the shrinkage of the desiccated dauer larvae of *lea-1* deletion mutant.

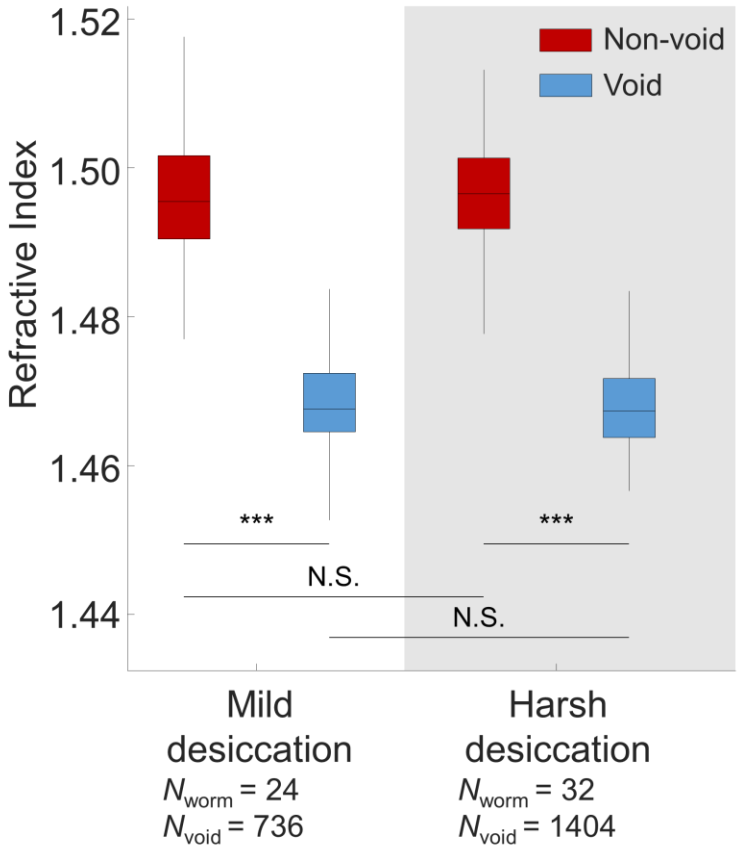

Supplementary Figure 6. Refractive index in void regions and their periphery of *lea-1* deletion mutant during mild and harsh desiccation conditions.

Supplementary Movie 1. Visualization of the RI tomogram and rendered isosurface of a typical *C. elegans* larva at the L3 stage.

Supplementary Movie 2. Visualization of the RI tomogram and rendered isosurface of a typical *C. elegans* dauer larva of controls after harsh desiccation (60% RH).

Supplementary Movie 3. Visualization of the RI tomogram and rendered isosurface of a typical *C. elegans* dauer larva of trehalose deletion mutants *daf-2;ΔΔtps* after harsh desiccation (60% RH).

Supplementary Movie 4. Visualization of the RI tomogram and rendered isosurface of a typical *C. elegans* larva of *lea-1* deletion mutants *daf-2;lea-1* after harsh desiccation (60% RH).

Supplementary References

1. P. Y. Liu, et al., Cell Refractive Index for Cell Biology and Disease Diagnosis: Past, Present and Future. *Lab Chip* **16**, 634–644 (2015).
2. M. Schürmann, et al., Three-dimensional correlative single-cell imaging utilizing fluorescence and refractive index tomography. *J. Biophotonics* **11**, e201700145 (2018).
3. S. Abuhattum, et al., Intracellular Mass Density Increase Is Accompanying but Not Sufficient for Stiffening and Growth Arrest of Yeast Cells. *Front. Phys.* **6**, 131 (2018).
4. Y. Park, et al., Refractive index maps and membrane dynamics of human red blood cells parasitized by Plasmodium falciparum. *Proc. Natl. Acad. Sci.* **105**, 13730–13735 (2008).
5. J. Aizenberg, V. C. Sundar, A. D. Yablon, J. C. Weaver, G. Chen, Biological glass fibers: Correlation between optical and structural properties. *Proc. Natl. Acad. Sci.* **101**, 3358–3363 (2004).
6. J. M. Soto, J. A. Rodrigo, T. Alieva, Label-free quantitative 3D tomographic imaging for partially coherent light microscopy. *Opt. Express* **25**, 15699–15712 (2017).
7. I. Y. Yanina, E. N. Lazareva, V. V. Tuchin, Refractive index of adipose tissue and lipid droplet measured in wide spectral and temperature ranges. *Appl. Opt.* **57**, 4839–4848 (2018).
8. Arwin, H. Optical Properties of Thin Layers of Bovine Serum Albumin, γ-Globulin, and Hemoglobin. *Appl. Spectrosc.* **40**, 313–318 (1986).
9. Wang, X. J., Milner, T. E., Chang, M. C. & Nelson, J. S. Group refractive index measurement of dry and hydrated type I collagen films using optical low-coherence reflectometry. *J. Biomed. Opt.* **1**, 212–216 (1996).
10. Bucciarelli, A. *et al.* A comparative study of the refractive index of silk protein thin films towards biomaterial based optical devices. *Opt. Mater. (Amst).* **78**, 407–414 (2018).